50th AIAA Aerospace Sciences Meeting including the New Horizons Forum and Aerospace Exposition
09 - 12 January 2012, Nashville, Tennessee

AIAA 2012-0076

Nonlinearity Identification and Flow Control for Low-Reynolds Number Aerodynamics with Unsteady Free-Stream

Young-Chang Cho[*1] and Wei Shyy[†1,2]
[1]*Department of Aerospace Engineering, University of Michigan, Ann Arbor, MI, 48109*
[2]*Hong Kong University of Science and Technology, Clear Water Bay, Hong Kong*

Effective control of unsteady aerodynamics depends on satisfactory treatment of fluid physics along with robust control techniques. For low-Reynolds number flyers operating at a chord Reynolds number of 10^4 or lower (hummingbird-size or smaller), due to their small size, light weight and low flight speed, it is critical for the control scheme to be effective in unsteady free-stream. In this study, a flow control framework based on linear system parameters, a penalty-based adaptive law, and dielectric barrier discharge (DBD) actuator is applied for a stationary wing at the chord Reynolds number of 1000. Special focus is on the nonlinearity associated with unsteady flow separation subject to substantial unsteady free-stream. The nonlinearity is reflected by the actuator saturation due to the breakdown voltage of the DBD actuator, vortex evolution/shedding, and the interaction between the separated flow and the free-stream. Its implications including fluctuations in lift and drag are investigated. The insight gained enables us to better manage parametric changes due to the unsteady flow environment, resulting in more effective flow control.

Nomenclature

c	=	airfoil chord length
C_d	=	sectional drag coefficient
C_l	=	sectional lift coefficient
C_{lt}	=	target lift coefficient
d	=	insulator thickness or relative degree
E or E_i	=	electric field vector
$\mathbf{F_b}$ or F_{bi}	=	quasi-steady body force from the DBD actuator
H_i	=	i-th Markov parameter
K_u	=	scaling factor for the control signal
K_z	=	scaling factor for the performance
n_c	=	order of the controller
Re	=	Reynolds number
t^*	=	normalized time (= $U_\infty t/c$)
T^*	=	normalized disturbance period (= $U_\infty T/c$)
U_∞	=	free-stream speed (= $\sqrt{U_x^2 + U_y^2}$)
$u(k)$	=	control signal at k-th control-time step
V_{app}	=	voltage applied to the DBD actuator
V_{app0}	=	nominal voltage applied to the DBD actuator
x_{act}	=	distance to the DBD actuator from the leading edge
$z(k)$	=	performance (= measurement) at k-th control-time step
z_{NMP}	=	real nonminimum-phase zero
α	=	angle of attack

[*] Postdoctoral Research Fellow, AIAA Member.
[†] Provost & Chair Professor, Department of Mechanical Engineering, Hong Kong University of Science and Technology, also Adjunct Professor, Department of Aerospace Engineering, University of Michigan, AIAA Fellow.

α_d = amplitude of sinusoidal disturbance in y-directional free-stream velocity
α_l = learning rate of the adaptive controller

I. Introduction

COMPARED to manned air vehicles, with the Reynolds number of 10^6 or higher, the flight performance of low-Reynolds-number flyers, with Reynolds numbers lower than 10^4, are more susceptible to unsteady aerodynamics due to their small size, light weight and low flight speed. For example, gusty environment along with unsteady flow separation can cause catastrophic changes in flight dynamics of such low-Reynolds-number flyers. Natural flyers, such as birds and insects, are well known for their superb maneuverability[1], because of their ability to utilize unsteady aerodynamics among other reasons. In addition to deeper understanding of low-Reynolds number aerodynamics, flow control can help mitigate various flight uncertainties and flow unsteadiness.

Recent progress in actuator technologies has offered opportunities to facilitate flow control. Among various actuators developed[2], the dielectric barrier discharge (DBD) actuator[3, 4] has been focused on as a promising control device for many applications. The DBD actuator can generate a thin layer of wall jet by delivering momentum to the neutral flow field from non-thermal ionized particles using a high intensity electric field. Although there are challenges in utilizing such technologies for small payload applications, such as power supply and weight, DBD actuator's advantages – simple structure, easy installation, and capability of high-frequency actuation – are attractive to low-Reynolds number applications.

Due to the non-obtrusive installation and operation potentialities of the DBD actuator, it has been studied widely to substitute mechanical actuators aiming to enhance aerodynamic lift, to reduce flow separation, or to prevent wing stall[5-7]. Considering the relatively low control authority of the DBD actuator compared to traditional actuators, there has been a great interest to improve its force generation or power efficiency and to increase the impact of actuation on the targeted flow. Recent efforts in this regard include manipulating the actuator's geometry[8, 9], probing operation regimes by changing the input voltage waveform[10], and finding optimal positions for the DBD actuator where desired performances can be maximized[11].

On the other hand, the capability of its responsive operation suggests that the DBD actuator is a promising device for controlling noise and low-Reynolds number aerodynamics. Some examples are tonal and/or broadband noise reduction in cavity flow, jet noise control, and mitigation of the influence of disturbance on lifting surface. In addition, the DBD actuator providing large bandwidth without mechanical complexity, which helps address multi-time scale physics[12] and manipulation of unsteady flow structures[13].

Recent advances notwithstanding, flow control remains a challenging area due to high dimensionality and nonlinearity inherent to flow systems of practical interest. The difficulties in essence are how to handle the system's nonlinearity and multiple time and length scales. Two common approaches are 1) to rely on a model reduction process to substantially decrease the dimensionality of the flow system[14, 15], and 2) to focus on its input (actuation)-to-output (measurement) relation based on generic dynamical models[5, 16]. Regardless of the modeling approach, nonlinearity of the flow system should be properly addressed–for example, the introduction of piecewise linear models[17] or adaptive processes[15, 18].

In our previous work[19, 20], an adaptive flow control framework is introduced to mitigate the influence of moderate free-stream disturbances, around several % variations in the vertical free-stream velocity, on a wing with the SD7003 airfoil geometry at the chord Reynolds number of 1000. Assuming a linearized transfer function from the control (actuation voltage) to measurement (lift or drag) of the flow-actuator system, the system parameters required by the controller − the first nonzero Markov parameter (i.e., the initial nonzero response to an impulse) and nonminimum-phase (NMP) zeros (i.e., unstable zeros[21]) of the linearized transfer function – are identified by using impulse response tests. The retrospective cost adaptive control (RCAC) algorithm[21], which minimizes the quadratic function based on the recomputed past inputs as well as the actual past control inputs and measurements, can stabilize the aerodynamic lift at the angle-of-attack of 15˚ where a massive flow separation appears. It is also shown that the system parameters are functions of the actuator location, actuation voltage, free-stream magnitude/direction, and Reynolds number, which can engender control difficulties or failure under significant flow unsteadiness. Furthermore, the scheduled variation of the system parameters based on multiple static identifications shows only a marginal improvement[19].

A larger number of parameter estimation methods for system identification are based on the least squares (LS) method[22], which estimates unknown parameters that minimize the quadratic criterion of the difference between the measurement and prediction. It is also well known that a persistent excitation signal (i.e., input having sufficient frequency content) is required to ensure estimation accuracy. Although the impulse response of a system can be

successfully used to estimate system parameters as in the previous work, system identification techniques using non-impulse excitations are necessary especially when the system parameters need to be estimated in real time and/or time-varying system parameter estimates are required. In such a case, non-batch regression techniques such as the recursive least squares (RLS) method[22, 23] can be useful.

In order to develop an effective flow control framework, the current study probes actuator dynamics and flow physics of a canonical problem, which is the rejection/mitigation of the impact of unknown wind gusts on aerodynamic lift using a DBD actuator. Focusing on the unsteady aerodynamics of the same wing and the Reynolds number as the previous work but subject to substantially higher disturbance magnitudes, around 30% of the vertical free-stream speed, the objectives of this paper are 1) to clarify the roles of nonlinearity causing the performance deterioration or failure of the control system, and 2) to enhance control effectiveness under such unsteady free-stream conditions. Particularly, the link between unsteady aerodynamics and the linearized flow-actuator model is explored by applying a recursive regression technique for different disturbance conditions. The contents of this paper are four parts: in sections II and III, models for flow simulation, system identification process, and control theory are summarized; Section IV includes A) investigation of key flow physics and nonlinearities under free-stream unsteadiness B) system identification, C) demonstration of closed-loop control results, and D) control with a time-varying NMP zero. Finally, the results and key findings are summarized in Section V.

II. Aerodynamics and DBD Actuator Models

For the numerical simulation of the flow-actuator system, the same models as Ref. 24 are used in this study. For clarity, they are summarized in this section.

A. Fluid Dynamics Model

The flow fields are analyzed by solving the incompressible Navier-Stokes equations using the Loci-STREAM[25], a parallelized pressure-based unstructured finite volume code. Since the ion and electron states are non-equilibrium and the ion temperature is comparable to the neutral fluid, the neutral fluid is treated as being isothermal. Considering the time scale disparity between the flow and the radio frequency (RF) actuator operation, the force acting on the neutral fluid is assumed to be a quasi-steady body force. The body force felt by the neutral flow is equivalent to the Lorentz force acting on the net charge density. For the unsteady operation of the actuator only the amplitude variation of the operation voltage with time scales much larger than the RF operation is considered. In index notation, the relevant conservation equations are

$$\frac{\partial u_j^*}{\partial x_j^*} = 0, \tag{1}$$

$$\frac{\partial u_i^*}{\partial t^*} + \frac{\partial \left(u_i^* u_j^*\right)}{\partial x_j^*} = F_{bi}^* - \frac{\partial p^*}{\partial x_i^*} + \frac{1}{Re}\frac{\partial}{\partial x_j^*}\left(\frac{\partial u_i^*}{\partial x_j^*}\right), \tag{2}$$

where, i, j=1,2 for 2-dimensional flow field. Here, F_{bi}^* is DBD body force vector defined below, $x_i^* = x_i/c$ is the Cartesian position in the global coordinate system, $u_i^* = u_i/U_\infty$ is the flow velocity, $p^* = (p - p_\infty)/\rho U_\infty$ is the pressure, all in normalized quantities, and $Re = \rho U_\infty c/\mu$ is the Reynolds number (c is the wing chord length, U_∞ is the free-stream speed, p_∞ is the free-stream pressure, ρ is the air density, and μ is the dynamic viscosity of air). The time resolution for the flow simulations is $\Delta t_f^* = U_\infty \Delta t_f / c = 0.05$, where Δt_f is the dimensional time resolution, while the control time step is $\Delta t_c^* = 10\Delta t_f^*$. As an example, for a chord of 5 cm in a free-stream speed of 0.3 m/s, which corresponds to Re = 1000, the flow time resolution and the control time resolution are 8 milliseconds and 0.08 second, respectively.

The flow-actuator system is composed of the SD7003 airfoil in free-stream and the DBD actuator attached on its upper surface near the leading edge. The angle-of-attack is 15°, which incorporates significant flow separation and instability in the separated flow without actuation[24], and Reynolds number is 1000. For the free-stream disturbance, the free-stream is assumed to be spatially uniform but with the sinusoidal unsteadiness in the y-direction, such as $\mathbf{U}(t^*) = \left(U_x, U_y\left(1 + \alpha_d \sin(2\pi t^*/T^*)\right)\right)$, where α_d is the disturbance amplitude, and T^* is the normalized disturbance period. The disturbance amplitude and period can be related to the Strouhal number $St \triangleq (\alpha_d U_\infty \sin\alpha)/U_\infty \simeq \alpha\alpha_d$ and reduced frequency $k \triangleq \pi T^{-1}/(U_\infty/c) = \pi/T^*$.

B. DBD Actuator Model

The DBD actuator model is a simplified model with linear electric field and constant net charge density[23, 26]. As shown in Figure 1, this model prescribes localized body forces in a triangular plasma region bounded by two electrodes and the dielectric surface. The electric field distribution inside the plasma region is approximated by spatially linear relations

$$\mathbf{E}'(x', y', t) = \left(\frac{\left|\mathbf{E}'(x', y', t)\right| k_2}{\sqrt{k_1^2 + k_2^2}}, \frac{\left|\mathbf{E}'(x', y', t)\right| k_1}{\sqrt{k_1^2 + k_2^2}} \right), \tag{3}$$

$$\left|\mathbf{E}'(x', y', t)\right| = E_0(t) - k_1 x' - k_2 y', \quad E_0(t) = \frac{V_{app}(t)}{d}, \tag{4}$$

where (x', y') is the actuator local coordinate system, d is the insulator thickness, and k_1 and k_2 are the linearized slopes of the electric field in the x' and y' directions, respectively. This is a solution of Gauss' equation with the constant net charge density assumption. In (4), the maximum electric field intensity E_0 is defined based on the applied voltage to the exposed electrode $V_{app}(t)$, which implies the amplitude modulation of the radio frequency AC voltage, and the slopes k_1 and k_2 of the electric field attenuation away from the exposed electrode and dielectric surface are set to allow the breakdown voltage at the boundary with the minimum electric field strength. As defined in the next section, the applied voltage is the scaled control signal and bounded by the breakdown voltage. Under feedback control, the applied voltage is changed depending on the control signal, resulting in a time-varying body force. As shown in Ref. 23, this analytical-empirical model results in a body force component acting on the fluid, given by

$$\mathbf{F}_b(x, y, t) = \rho_c q_c \delta(x, y) f_v \Delta t_d \mathbf{E}(x, y, t), \tag{5}$$

where f_v is the AC frequency of the voltage applied to the DBD actuator and Δt_d is the discharge duty cycle, and $\mathbf{E}(x,y,t)$ is the electric field distribution (3) transformed to the global coordinate system. Furthermore, since the constant charge density ρ_c with unit charge q_c is present only inside the plasma region, $\delta(x,y)$ is set to 0 or 1 depending on the position. For this study, the active plasma region is given by the triangular region, shown in Figure 1, where the horizontal electric field length $l_h = 0.05c$ and vertical length $l_v = 0.025c$.

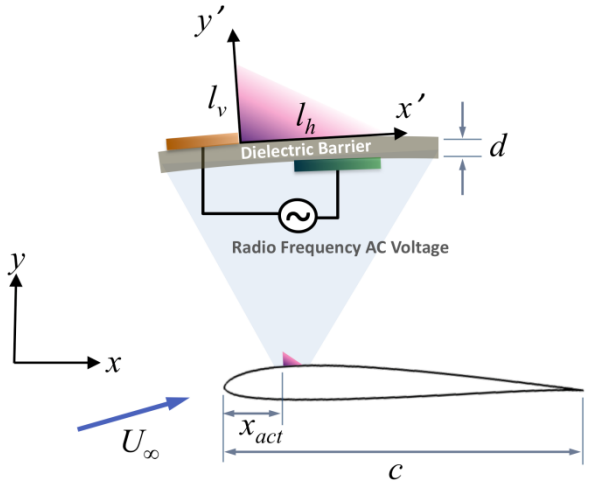

Figure 1. Schematics of the DBD actuator model on the SD7003 airfoil.

The discharge duty cycle is the portion of time during which effective force generation occurs in each operation cycle. Since the reduced-order DBD model (3)–(5) is based on the quasi-steady assumption using the time scale disparity, the control input is meaningful when its timescale lies between those of low Reynolds number flow and plasma operation. The simplified DBD model has been validated against experimental data of force generation[27] and maximum induced flow velocity[28]. Although this simplified model captures some main features of DBD's actuation

characteristics, a further improved model can replace it without impacting the main aspects of the framework. In this study, only a single co-flow directional DBD actuator and the position of the actuator at $x_{act}/c = 0.2$ are considered.

III. System Identification and Control

C. Recursive Least Squares (RLS) Method

As described in Ljung and Soderstrom[22], the output $y(k)$ of a linear, time-invariant system at k-th time step can be expressed with the regression relation

$$y(k) = \theta^T \varphi(k) + \nu(k), \tag{6}$$

where $\varphi(k)$ is the regressor vector composed of input and output data, θ is the unknown system parameter vector, and $v(k)$ is the prediction error or noise. Then, by minimizing the prediction error between the unknown parameters and their estimates using a least squares function, the system parameter vector for $k = N$ can be estimated as

$$\hat{\theta}(N) = \left[\sum_{k=1}^{N} \alpha_k \varphi(k) \varphi^T(k)\right]^{-1} \sum_{k=1}^{N} \alpha_k \varphi(k) y(k). \tag{7}$$

where α_k is the weighting factor that can handle the amount of each sample's contribution to the parameter estimates. Instead of using the whole set of input and output data, a recursive system-identification algorithm seeks the system parameters by updating the estimates of the parameters using an input-output pair at each time step. Since a specific mode of a system can or cannot be excited depending on the input signal, the choice of an appropriate input signal is critical. In order to provide a broad bandwidth input signal, the white noise signal, which is a random signal having constant probability density in frequency domain up to the Nyquist frequency, is used in this study. By introducing a recursive formulation, the system parameter vector can be updated with the measurement at each time step by

$$\hat{\theta}(k) = \hat{\theta}(k-1) + L(k)\left[y(k) - \hat{\theta}^T(k-1)\varphi(k)\right], \tag{8}$$

$$L(k) = \frac{P(k-1)\varphi(k)}{{}^{1}/_{\alpha_k} + \varphi^T(k)P(k-1)\varphi(k)}, \tag{9}$$

$$P(k) = P(k-1) - \frac{P(k-1)\varphi(k)\varphi^T(k)P(k-1)}{{}^{1}/_{\alpha_k} + \varphi^T(k)P(k-1)\varphi(k)}. \tag{10}$$

The initial values can be chosen as $P(0) = cI$ and $\hat{\theta}(0) = 0$ with a large constant c for a faster decay of the effect of initial values.

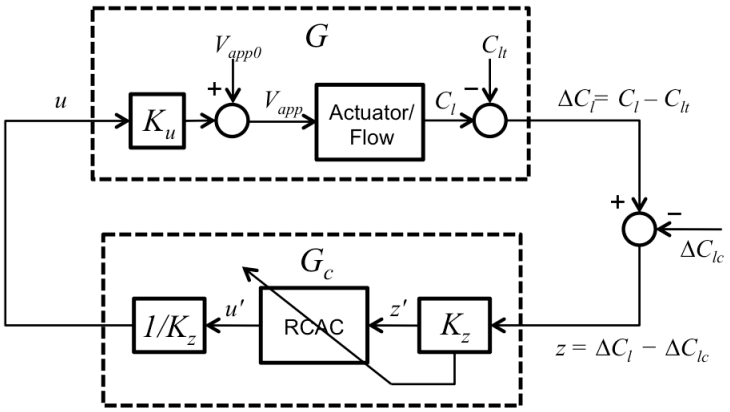

Figure 2 Flow-actuator system G and adaptive controller G_c (V_{app0}: nominal voltage, V_{app}: DBD actuation voltage, C_l: lift coefficient, C_{lt}: target lift coefficient, ΔC_{lc}: commanded lift change, K_u and K_z: scaling factors).

D. Retrospective Cost Adaptive Algorithm

The block diagram of the flow-actuator system and controller is shown in Figure 2. The controller G_c takes the difference between the current lift change ΔC_l and the commanded lift change ΔC_{lc} as the measurement, which is equal to the performance. In order to scale variables for the controller and for the actuator, two scaling factors K_z and K_u are introduced, respectively. This scaling helps to keep the control and the performance to be in the same range, which can significantly affect the control performance. Furthermore, the scaling relieves the performance dependency on the tunable parameter in the controller, namely the learning rate that is introduced below. For the controller, the retrospective cost adaptive control (RCAC) algorithm presented in Ref. 21 is summarized in this section for a single-input, single-output control system along with some modifications for the scaling.

Consider the single-input, single-output linear discrete-time system

$$x(k+1) = Ax(k) + Bu(k) + D_1 w(k), \tag{11}$$

$$z(k) = E_1 x(k) + E_0 w(k), \tag{12}$$

where $x(k) \in \mathbb{R}^n,\ z(k) \in \mathbb{R},\ u(k) \in \mathbb{R},\ w(k) \in \mathbb{R}^{l_w}$ are the state, performance, control, and exogenous command and/or disturbance signal with $k \geq 0$. In this paper, an adaptive output feedback controller presented below minimizes the performance variable z in the presence of the exogenous signal w, which could be a disturbance, command, or both. The difference between lift or drag coefficient of the airfoil and its nominal value is set as the performance, which is minimized when there is a sinusoidal disturbance in the free-stream flow.

For the general control problem given by (11)–(12), we use a strictly proper time-series controller of order n_c, such that the control $u(k)$ is given by

$$u'(k) = \sum_{i=1}^{n_c} M_i(k) u'(k-i) + \sum_{i=1}^{n_c} N_i(k) z'(k-i), \tag{13}$$

where, for all $i = 1, \cdots, n_c$, $M_i(k), N_i(k) \in \mathbb{R}$ are given by the adaptive law presented below. The control can be expressed as

$$u'(k) = \theta^T(k)\, \phi'(k), \tag{14}$$

where

$$\theta(k) \triangleq \begin{bmatrix} N_1(k) & \cdots & N_{n_c}(k) & M_1(k) & \cdots & M_{n_c}(k) \end{bmatrix}^T, \in \mathbb{R}^{2n_c} \tag{15}$$

is the controller parameter matrix, and the regressor vector $\phi'(k)$ (and $\phi(k)$) is given by

$$\phi'(k) \triangleq \begin{bmatrix} z'(k-1) \\ \vdots \\ z'(k-n_c) \\ u'(k-1) \\ \vdots \\ u'(k-n_c) \end{bmatrix} = K_z \begin{bmatrix} z(k-1) \\ \vdots \\ z(k-n_c) \\ u(k-1) \\ \vdots \\ u(k-n_c) \end{bmatrix} \triangleq K_z \phi(k) \in \mathbb{R}^{2n_c}. \tag{16}$$

For positive integer μ, we define the extended control vector $U'(k)$ (and $U(k)$) by

$$U'(k) \triangleq \begin{bmatrix} u'(k) \\ \vdots \\ u'(k-p_c+1) \end{bmatrix} = K_z \begin{bmatrix} u(k) \\ \vdots \\ u(k-p_c+1) \end{bmatrix} \triangleq K_z U(k) \in \mathbb{R}^{p_c}, \tag{17}$$

where $p_c \triangleq \mu + 1$. From (14), it follows that the extended control vector $U'(k)$ can be written as

$$U'(k) \triangleq K_z \sum_{i=1}^{p_c} L_i \theta^T(k-i+1) \phi(k-i+1), \tag{18}$$

where

$$L_i \triangleq \begin{bmatrix} 0_{(i-1)\times 1} \\ 1 \\ 0_{(p_c-i)\times 1} \end{bmatrix} \in \mathbb{R}^{p_c}. \tag{19}$$

Next, define the retrospective performance

$$\hat{z}\big(\hat{\theta}, k\big) \triangleq z'(k) - \bar{B}_{zu}\left(U'(k) - \hat{U}\big(\hat{\theta}, k\big)\right), \tag{20}$$

where $\hat{U}(\hat{\theta}, k) \triangleq K_z \sum_{i=1}^{p_c} L_i \hat{\theta}^T \phi(k-i+1)$, $\hat{\theta} \in \mathbb{R}^{2n_c}$ is an optimization variable, and control matrix $\bar{B}_{zu}$ is given by Eq. (30) below. Note that $\hat{z}\big(\hat{\theta}, k\big)$ is obtained by modifying the performance variable $z(k)$ based on the difference between the actual past control inputs $U(k)$ and the recomputed past control inputs $\hat{U}\big(\hat{\theta}, k\big)$ assuming that $\hat{\theta}$ had been used in the past. Thus, $\hat{z}\big(\hat{\theta}, k\big)$ may be interpreted as an approximation of the performance had $\hat{\theta}$ been used in the past.

Now, consider the retrospective cost function

$$\hat{J}(\hat{\theta}, k) \triangleq \hat{z}^2(\hat{\theta}, k) + \alpha_l(\hat{\theta} - \theta(k))^T(\hat{\theta} - \theta(k)), \tag{21}$$

where the learning rate α_l affects the transient performance and the convergence speed of the adaptive control algorithm. Substituting (20) into (21) yields

$$\hat{J}(\hat{\theta}, k) = \hat{\theta}^T A(k)\hat{\theta} + b^T(k)\hat{\theta} + c(k), \tag{22}$$

where

$$A(k) \triangleq D^T(k)D(k) + \alpha_l I, \tag{23}$$

$$b(k) \triangleq 2K_z D^T(k)\big(z(k) - \bar{B}_{zu}U(k)\big) - 2\alpha_l\theta(k), \tag{24}$$

$$c(k) \triangleq K_z^2\big(z(k) - \bar{B}_{zu}U(k)\big)^2 + \alpha_l\theta^T(k)\theta(k), \tag{25}$$

and $D(k) \triangleq K_y \bar{B}_{zu} \sum_{i=1}^{p_c} \big(L_i \phi^T(k-i+1)\big)$. Here, the learning rate is defined as $\alpha_l \triangleq K_z^2$ for an appropriate scaling. Since $A(k)$ is positive definite, $\hat{J}\big(\hat{\theta}, k\big)$ has a unique global minimizer, which can be used for the update law

$$\theta(k+1) = -\frac{1}{2}A^{-1}(k)b(k). \tag{26}$$

The adaptive controller (14) and (23)–(26) requires limited model information of the plant (11)–(12); however, the controller does require knowledge of $\bar{B}_{zu}$, which is constructed using estimates of the plant's relative degree, first nonzero Markov parameter, and the nonminimum-phase (NMP) zeros of the transfer function from *u* to *z*. Markov parameters are the impulse response of a discrete-time linear time-invariant system, and they are very functional in system identification especially due to their uniqueness to the system. On the other hand, NMP zeros are zeros of the rational transfer function that lie outside the unit circle in the complex domain. Though the latter is sometimes called unstable zeros, they are not a measure of the system's stability. Instead, it is known that a NMP system incurs a fundamental limitation in feedback control performance[29]. In addition, an odd number of real NMP zeros in continuous-time systems are responsible for and related to the initial undershoot[30], which are also observed for the current flow-actuator system as shown in the previous study[20].

In order to construct the control matrix using aforementioned system parameters, consider the transfer function from *u* to *z* given by

$$G_{zu}(z) \triangleq E_1(zI - A)^{-1}B, \tag{27}$$

which can be written as

$$G_{zu}(z) \triangleq H_d \frac{\beta(z)}{\alpha(z)}, \tag{28}$$

where the relative degree $d \geq 1$ is the smallest positive integer i such that the i-th Markov parameter $H_i \triangleq E_1 A^{i-1} B$ is nonzero, and $\alpha(z)$ and $\beta(z)$ are monic coprime polynomials. Next, let $\beta(z)$ have the factorization

$$\beta(z) \triangleq \beta_s(z)\beta_u(z), \tag{29}$$

where $\beta_s(z)$ is a monic polynomial of degree n_s whose roots lie inside the unit circle, and $\beta_u(z)$ is a monic polynomial of degree n_u whose roots lie on or outside the unit circle. Furthermore, we can write $\beta_u(z) = z^{n_u} + \beta_{u,1} z^{n_u-1} + \cdots + \beta_{u,n_u-1} z + \beta_{u,n_u}$. Then we let $\mu = n_u + d$ and the resulting control matrix $\bar{B}_{zu}$ is given by

$$\bar{B}_{zu} \triangleq H_d \begin{bmatrix} 0_{1\times d} & 1 & \beta_{u,1} & \cdots & \beta_{u,n_u} \end{bmatrix} \in \mathbb{R}^{1\times p_c}. \tag{30}$$

Note that $\bar{B}_{zu}$ is constructed using knowledge of the relative degree d, the first nonzero Markov parameter H_d, and the nonminimum-phase zeros of $\beta_u(z)$ of the transfer function from u to z.

The first nonzero Markov parameter and NMP zeros of a linear model can be estimated by using the impulse response (i.e., Markov parameters) of the model. When the RLS method is used to estimate the system parameter vector in (6), the impulse response of the linearized flow-actuator system is obtained by using the estimated discrete time model. Our previous study[20] showed that the flow-actuator system is a nonminimum-phase system with the relative degree of 1, meaning that the system has a reverse initial response with one step time lag. Accordingly, based on the parameter scaling using $K_z = 1$ and $K_u = 10^4$, the first nonzero Markov parameter and the learning rate are –1 and 1, respectively, and only one real NMP zero is estimated for system identification.

In order to stabilize the lift fluctuation, as shown in Figure 2, the performance is defined as the difference between the instantaneous lift coefficient C_l and a target lift coefficient C_{lt}, i.e., the commanded lift change ΔC_{lc} is set to 0. Although it is reasonable as a target to use the nominal lift coefficient, which is the lift with nominal actuation but no disturbance, different targets are also used for the test cases because, as described with the results, the control performance is sensitive to the target lift. Since the actuation voltage V_{app} is limited by actuator saturation, the controller is informed its amplitude saturation[31]. As a result, the actual control $u(k)$ is chosen as $\max(u(k), u_{bd})$, where u_{bd} is the control that results in the breakdown voltage.

IV. Results and Discussion

A. Key flow physics and nonlinearities under free-stream unsteadiness

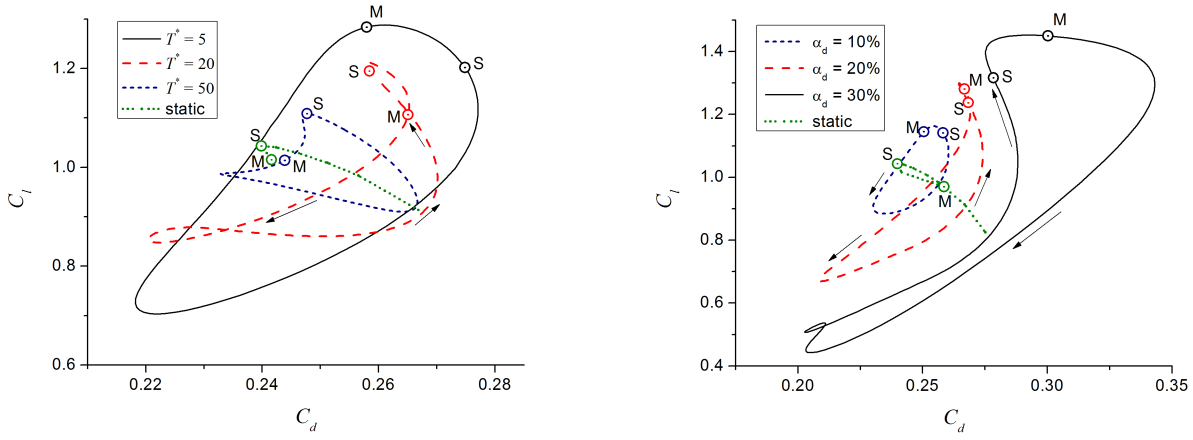

(a) $\alpha_d = 20\%$ ($St = 0.05$) (b) $T^* = 10$ ($k = 0.31$)

Figure 3. Lift-drag relation for one disturbance cycle ($\alpha = 15°$, open-loop control with the constant 2kV actuation): S is the static stall point, and M is where the disturbance velocity is maximum.

The unsteady free-stream with the disturbance changes both angle-of-attack and free-stream speed. As a result, the high-angle-of-attack airfoil experiences flow separation/reattachment and vortex evolution/shedding[20]. In order

to understand the flow physics in response to the disturbance with open-loop control (constant voltage actuation), the evolutions of aerodynamic forces for one disturbance cycle are shown in Figure 3. The lift-drag relations according to the disturbance period for the disturbance magnitude of 20% (St = 0.05) are shown in Figure 3(a) along with the static lift-drag relation that is obtained by changing the vertical free-stream velocity by up to ±20%. The influence of disturbance magnitude for the disturbance period of 10 (k = 0.31) is shown in Figure 3(b) along with the static lift-drag relation for up to ±30% free-stream change, and the points S and M correspond to the instants of stall and maximum y-directional velocity, respectively. As shown in Figure 3(a), the smaller the disturbance period becomes, the further the lift-drag relation deviates from the static relation. Furthermore, as the disturbance period decreases, the instant of maximum lift occurs later than the stall point S, which is an indication of delayed stall. The comparison also shows that there is a disturbance period (in this case T^* = 20) where the sudden lift loss due to stall is most significant, and for the even lower disturbance period T^* = 5 the lift-drag relation becomes circular, showing that the instant of maximum lift is close to the moment of maximum y-directional velocity.

In Figure 3(b), on the other hand, the increase of the disturbance magnitude significantly changes the shape and direction of the lift-drag path as well as the range of aerodynamic forces. Specifically, a higher disturbance magnitude results in more obvious delayed stall during which drag increases more dramatically. For α_d = 30%, the lift-drag totally drifts from the static lift-drag relation. On the other hand, through the most of the second half-cycle, which corresponds to the part of the lift-drag path with lift increase before S, the change in the disturbance magnitude has little effect on the shape of the path (i.e., the paths are parallel to each other in that part).

In Figure 4, flow fields at two time instants are compared for the 20% and 30% disturbance magnitudes. At instant M, compared to the 20% case, the case with the 30% disturbance magnitude (St = 0.08) shows a smaller attached flow region near the DBD actuator at x/c = 0.2 and larger vortex structures within the separated flow region due to the higher maximum y-directional free-stream velocity. As a result, a set of more massive vortices appears at the subsequent instant, which is $0.15T^*$ after instant M, as shown in Figure 4(d) compared to Figure 4(c). The larger and more complex separated flow structure for the case with α_d = 30% explains the larger lift and drag after stall as well as the reversed lift-drag path. As shown in detail in the following sections, the separated flow region develops into multiple shedding vortices that accompany significant lift variations.

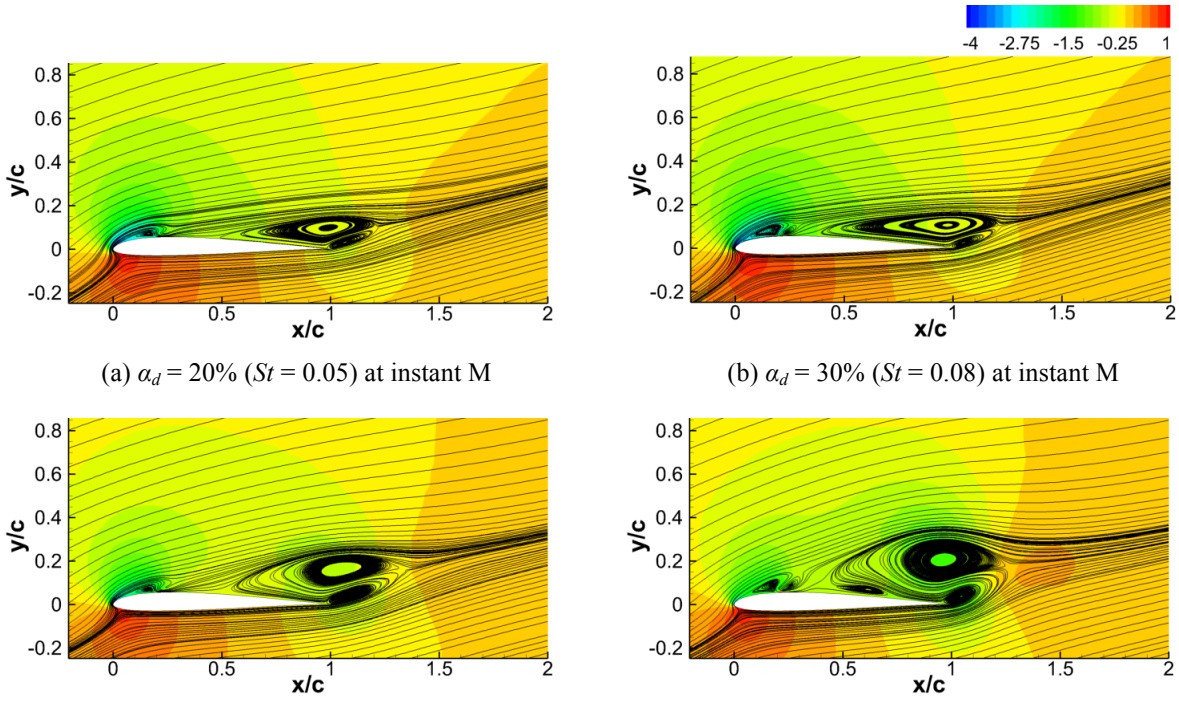

(a) α_d = 20% (St = 0.05) at instant M

(b) α_d = 30% (St = 0.08) at instant M

(c) $0.15T^*$ after (a)

(d) $0.15T^*$ after (b)

Figure 4. Streamlines and pressure coefficient contours at instant M in Figure 3 and after $0.15T^*$ (The DBD actuator is located at x/c = 0.2).

B. System Identification

Since the free-stream unsteadiness can cause significant changes in system's dynamics, a system identification (ID) method based on the static flow conditions, such as impulse response test, may not provide reliable parameter estimates, especially under substantial disturbance conditions. Alternative approaches are the identification methods based on white noise signals, such as the recursive least squares (RLS) method. Since the RLS method can update the parameter estimates based on each measurement, it can be applied for online system ID if sufficient data with persistent excitation is available. While applying the RLS method, one of the key issues is the convergence of system parameter estimates. As shown in Figure 5, the convergence of the system parameter estimates requires over 600 measurements for the case where the impulse response-based estimation have been done for around 100 measurements.

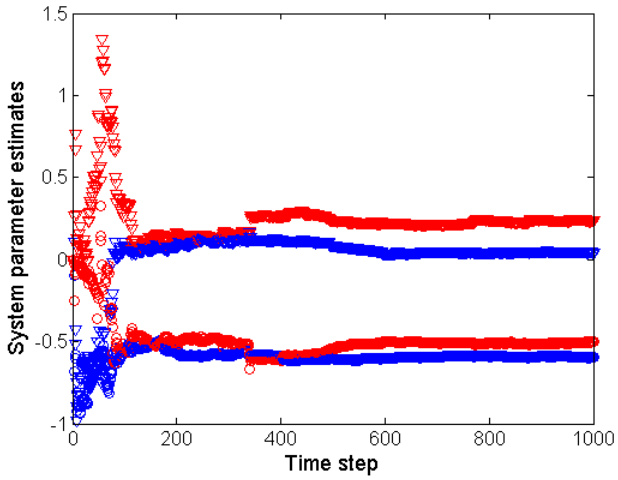

Figure 5 Convergence of 4 system parameter estimates out of 50 using the RLS method (actuation with 1 kV_{RMS} white noise, without disturbance, initialization with zeros).

In order to understand the impact of the free-stream unsteadiness on the system parameter estimates, time-averaged system parameter estimates can be obtained by applying the RLS method to the flow-actuator system with unsteady free-stream.

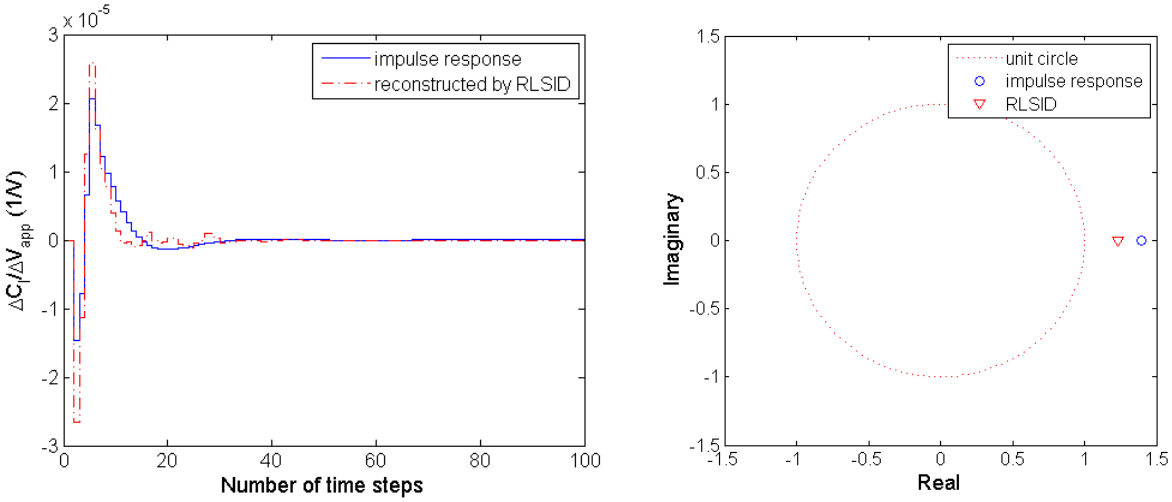

(a) Markov parameters (impulse response) (b) nonminimum-phase zero

Figure 6 Comparison between impulse response and system identification using the RLS method: the original impulse response is obtained by using a finite impulse of 0.2 kV with V_{app0} = 2 kV.

Before introducing the free-stream unsteadiness, the parameter estimates using the RLS method without disturbance are compared with the impulse response-based identification in Figure 6. In order to reconstruct the

impulse response using the RLS method, a 25th order infinite impulse response (IIR) filter with 1000 samples is used. Although the overall shape of reconstructed impulse response is comparable to the original impulse response, there are differences in the peak values and transient response. Furthermore, the estimated real nonminimum-phase (NMP) zero is smaller than the one from impulse response test. Although the difference is noticeable, considering the impulse response of the flow-actuator system is also sensitive to the impulse magnitude itself[20], such a difference is not unusual.

The same conditions for the RLS method are used for cases with the free-stream disturbance, and the convergence histories of 4 chosen system parameters are shown in Figure 7. Although the disturbance induces significant lift fluctuations for $T^* = 20$, it is interesting to observe the stable (and faster than the no disturbance case in Figure 5) convergence of the system parameters.

The parameter estimates using RLS for the cases with different disturbance conditions (no disturbance, $T^* = 50$, and $T^* = 20$) are compared in Figure 8. Even with such disturbance conditions, the reconstructed impulse responses are more consistent compared to the comparison between the original impulse and reconstructed one shown in Figure 6. Though the different impulse responses predict only real NMP zeros, it is difficult to observe any trend in the estimates of NMP zeros.

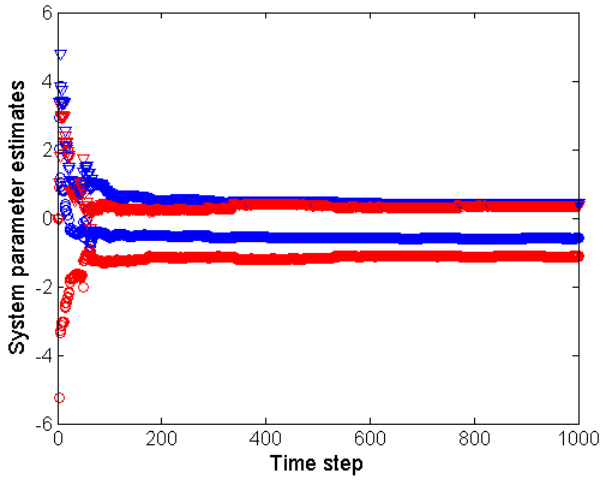

Figure 7 Convergence of 4 system parameter estimates out of 50 using the RLS method (actuation with 1 kV_{RMS} white noise, with disturbance of $T^* = 20$ ($k = 0.16$), initialization with zeros).

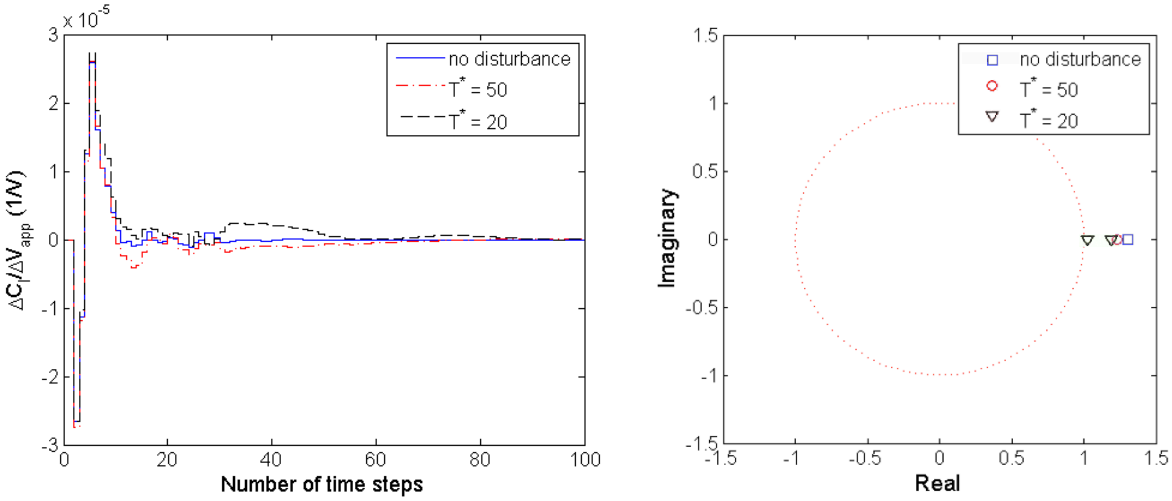

(a) Markov parameters (impulse response) (b) nonminimum-phase zero

Figure 8 System identification with and without disturbance using the RLS method.

As described in the previous section, the model parameters for the flow-actuator system are based on a linear time-invariant system. As a result, though the system dynamics can be highly nonlinear depending on the actuation and disturbance conditions, the system parameter estimates only represent the linearized model of the flow-actuator system in the sense of either time-averaged approximation through the accumulative process of the RLS method or small excitation around the nominal state with the nominal actuation voltage. Though the system parameters estimated by the RLS method with the disturbance effects are expected to incorporate the flow dynamics induced by the unsteadiness, which is absent in the estimation using impulse tests, some closed-loop control exercises show no better results than the cases with impulse-test-based parameter estimates. In fact, for the closed-loop control cases employed in the following section, the impulse test ID results in a better control performance with the RCAC algorithm in terms of either transient time or steady-state response. As a result, only impulse tests are used to estimate the parameters in section C. However, as shown in section D, the application of the RLS method to segmental data sets result in the time-varying parameter estimates, which can enhance the control performance for some test cases.

C. Closed-loop control result

In this section, the closed-loop control results based on the RCAC and the NMP zero estimated by the impulse test are demonstrated. In Figure 9, the time histories of steady-state drag coefficient, lift coefficient, and the actuation voltage for one disturbance period are shown along with the snapshots that compare open-loop and closed-loop flow fields at some selected time instants. For the disturbance with α_d = 30% (St = 0.08) and T^* = 5 (k = 0.63), the open-loop actuation of V_{app} = 2 kV results in the $O(1)$ variation of the lift coefficient and $O(0.1)$ of the drag coefficient. The flow field snapshots of open-loop control in the left column show the evolution and shedding of two neighboring vortices in response to the free-stream disturbance. The overall lift variation assimilates the sinusoidal waveform of the disturbance but with the phase-advanced minimum at about t^*/T^* = 0.7, which corresponds to the moment of vortex shedding as shown in the snapshots. Compared to the following cases with longer disturbance periods, this case shows the evolution of the separated flow structure in accordance with the free-stream unsteadiness.

The closed-control case (red line in the time history and right column in the snapshots) is for the target lift coefficient of 1.3. The reasons that target lift is set higher than the nominal lift coefficient are two: to decrease the possible actuator saturation time by shifting the actuation voltage to a higher level and to achieve a better control performance, which turns out to be dependent on the target value. Since the controller samples and outputs every 10th flow time step, there are 10 discrete voltage updates within one disturbance period. The voltage (or control) waveform is close to a sinusoid such as the lift variation except the $0.1T^*$ time lag. The maximum voltage occurs in the middle of the growth of the separated flow region, and the minimum voltage is applied after the moment of vortex shedding. Furthermore, since the controller tried to decrease the voltage lower than the breakdown voltage, there is voltage saturation in t^*/T^* = 0.7–0.9. As shown in the snapshots for the first half-cycle, the vortex evolution/shedding process existing in the open-loop case is substantially reduced. Even with the relatively low-time resolution, actuator saturation, and the remaining vortex structure through t^*/T^* = 0.9–0.15, the lift variation is successfully stabilized. The streamlines after t^*/T^* = 0.3 are attached on the airfoil without a noticeable difference for most of the second half-cycle. On the other hand, although the drag is not in the control objective, its fluctuation is decreased by the actuation for lift stabilization.

In Figure 10, the control result with a longer disturbance period of T^* = 10 (k = 0.31) is shown for one disturbance period. Compared to the case with T^* = 5, the open-loop lift variation shows a more deviation from the sinusoidal waveform, especially in the reduced-lift part that shows two lift dips before the lift recovery. The open-loop flow field snapshots show substantial flow separation with two large vortices whose shedding timings correspond to the first lift dip at t^*/T^* = 0.5 and the local maximum before the second dip at t^*/T^* = 0.55, respectively. There is a small consecutive vortex whose shedding is related to the second dip at t^*/T^* = 0.6.

The target lift for closed-loop control is 1.1 in this case. The closed-loop lift history in Figure 10 shows the lift fluctuation due to the disturbance is successfully suppressed except for t^*/T^* = 0.9–0.2 where the actuator saturation occurs. The voltage waveform is maximum at the moment of the first vortex shedding, which occurs approximately $0.2T^*$ later than the maximum open-loop lift. It is also interesting to observe that even for the similar amount of lift fluctuation, the maximum voltage required for lift stabilization is about 50% lower than the case with T^* = 5 in Figure 9. The closed-loop flow snapshots show that the size of the separated flow region is noticeably decreased compared to the open-loop case. Furthermore, the vortex evolution process becomes faster; as a result, vortex shedding occurs in the earlier stage of t^*/T^* = 0.2 compared to t^*/T^* = 0.5 for open-loop control. Similarly to the case with T^* = 5, the closed-loop actuation reduces the drag fluctuation, and its peak moments are related to the moments of vortex shedding and maximum voltage.

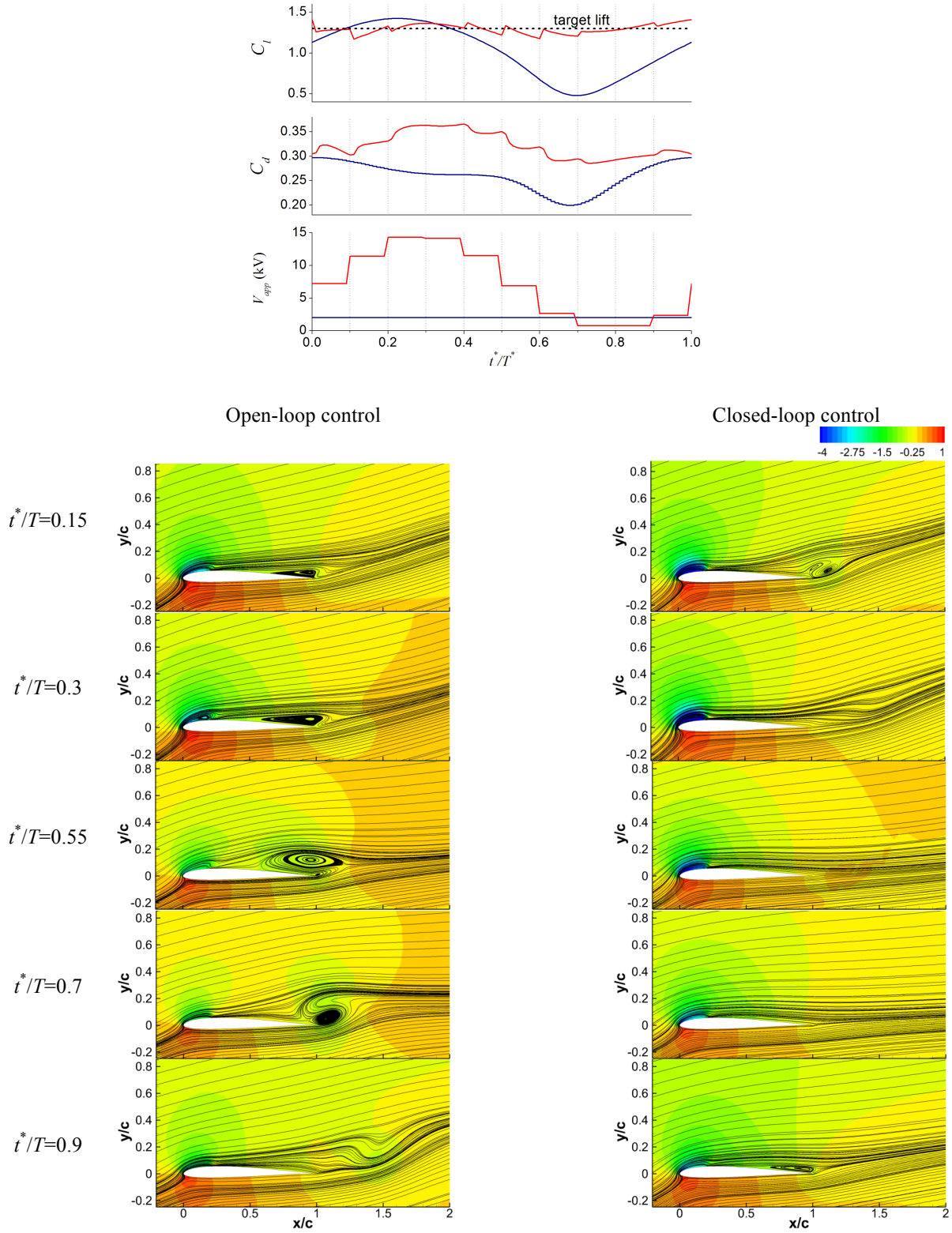

Figure 9 Time evolutions of aerodynamic forces (red: closed-loop, blue: open-loop) and flow field with streamlines and pressure coefficient contours: α_d = 30%, T^* = 5 (St = 0.08, k = 0.63).

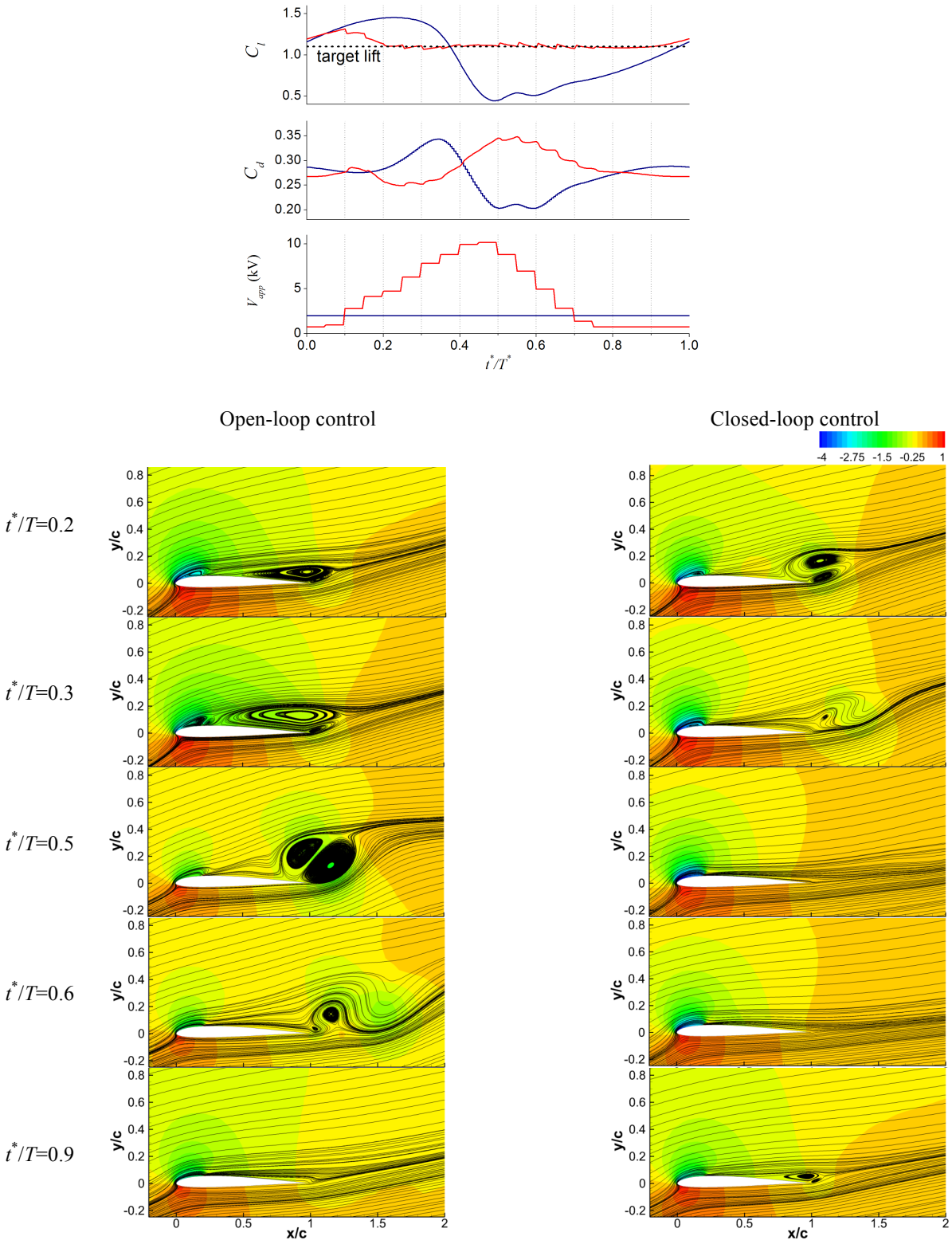

Figure 10 Time evolutions of aerodynamic forces (red: closed-loop, blue: open-loop) and flow field with streamlines and pressure coefficient contours: α_d = 30%, T^* = 10 (St = 0.08, k = 0.31).

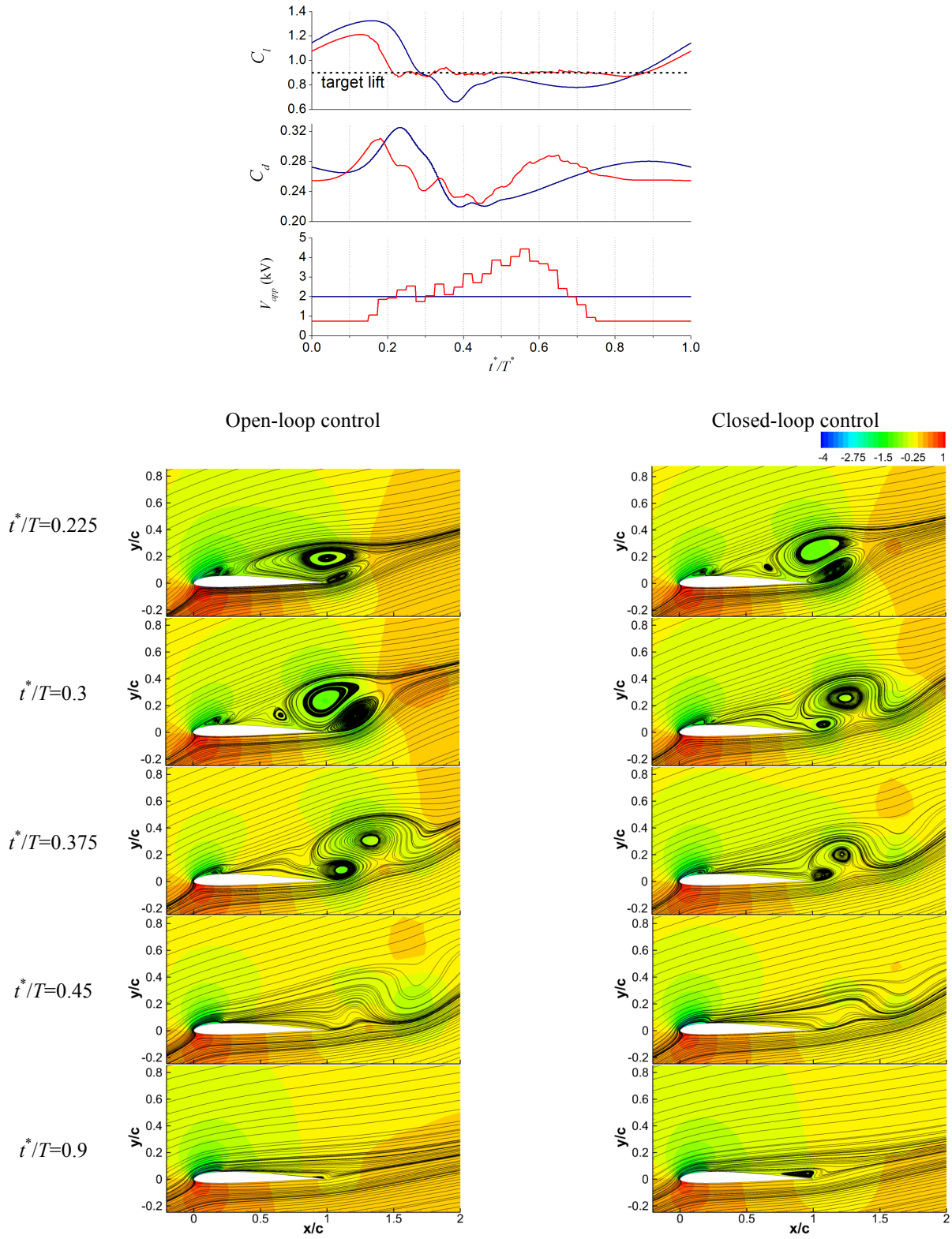

Figure 11 Time evolutions of aerodynamic forces (red: closed-loop, blue: open-loop) and flow field with streamlines and pressure coefficient contours: α_d = 30%, T^* = 20 (St = 0.08, k = 0.16).

The control result with the disturbance period of $T^* = 20$ ($k = 0.16$) is shown in Figure 11. The open-loop lift history shows multiple lift drops followed by the broad local lift minimum, which is caused by the second half-cycle of the sinusoidal disturbance. Compared to the cases with $T^* = 5$ and 10, the amplitude of the lift fluctuation is about 30% lower. The target lift for closed-loop control is 0.9 in this case; as a result, a larger portion of the period is subject to the actuator saturation. Similarly to the cases with lower disturbance periods, when the open-loop and closed-loop snapshots are compared, the controller decreases the size of vortex structures and advances their evolutions by $0.075T^*$ in this case. In addition, the closed-loop case involves a larger number of vortices with smaller sizes. Although the strong vortex shedding process persists even with the closed-loop actuation for $t^*/T^* =$ 0.225–0.375, the lift fluctuation is effectively suppressed by the controlled voltage.

D. Control with a time-varying nonminimum-phase zero

Although the cases chosen in section C demonstrate successful lift stabilization, the control performance is dependent on various parameters, such as the disturbance magnitude/period, nominal voltage, target lift, and controller parameters. Among them, the disturbance conditions are directly related to the flow structure and its evolution as described. In addition, the sensitivity to the target lift is another indication of nonlinearity in the flow-actuator system. They not only affect the amount of actuator saturation but also have significant effects on the flow dynamics.

As an example, Figure 12 shows the closed-loop control results for a same case but with different target lift coefficients, one with the nominal lift (lift with nominal actuation of V_{app0} but without disturbance) shown in (a) and the other with a lower value of 0.9 in (b). As apparent from the open-loop lift history for $t^* = 0$–150, the time-averaged lift coefficient 0.927 deviates from the nominal lift coefficient 1.03, which suggests an aspect of nonlinearity known as the nonlinear steady-state characteristic[32]. In Figure 12(a), although the case with the nominal lift as a target shows the reduced fluctuation amplitude with control, non-periodic oscillations persist around the target lift. On the other hand, for the case with a target lift coefficient of 0.9 in Figure 12(b), though the steady-state fluctuation magnitude becomes larger due to its longer actuator saturation because of the reduced target, the lift fluctuation is more bounded around the target for a significant portion of the disturbance period. This comparison indicates another nonlinearity in the problem, i.e., the target dependency of the controller's performance. The detailed mechanism causing this dependency needs further study.

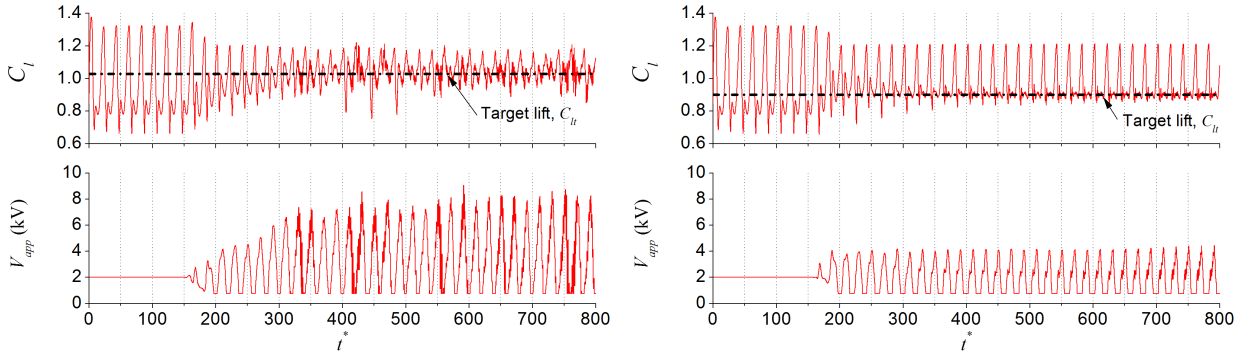

(a) $C_{lt} = 1.03$ (nominal lift coefficient) (b) $C_{lt} = 0.9$

Figure 12 Closed-loop lift control results with different targets: $\alpha_d = 30\%$, $T^* = 20$ ($St = 0.08$, $k = 0.16$).

As an effort to incorporate the influence of disturbance on the system parameter estimates, a series of impulse tests under different actuation and flow conditions is done in the previous study[19]. Although such an approach showed the potential parametric variations according to the free-stream condition, such as the increase of the real NMP zero for a higher y-directional free-stream velocity, it lacks the effect of the unsteady processes described in the previous section. In order to assess the system parameter variations with the existence of disturbance, the RLS method is applied for the concatenated sets of segmented data windows. First, white noise data is used as the actuation voltage while the flow-actuator system is under the influence of the free-stream disturbance. Then, as shown in Figure 13(a), each disturbance period is divided into 4 segments that roughly cover the 4 stages of flow evolution: i) the growth of flow separation (represented by $t^*/T = 0.225$ in Figure 11), ii) the lift dip due to vortex shedding ($t^*/T = 0.375$ in Figure 11), iii) the lift drop due to the decreasing y-directional free-stream velocity, and iv) the lift recovery due to the increasing disturbance velocity. Then, all the data windows of segment 1 are concatenated and the same for the rest 3 segments, resulting in 4 data sets corresponding to the 4 segments in one

disturbance period. Finally, the RLS method is used for each data set, and four NMP zero estimates are assigned to one disturbance period as shown in Figure 13(b).

Since the time resolution of the control/measurement is 10 times the flow simulation, for $T^* = 20$, the number of data points in one window is only 10, which is too small as shown in section B. However, since only one NMP zero is approximated from the estimated impulse response, the concatenated segmental data sets turn out to result in reasonable convergence. The NMP zero estimates for one disturbance cycle in Figure 13(b) shows a sudden increase in segment 2, which corresponds to the phase of vortex shedding as shown $t^*/T = 0.375$ in Figure 11. The results also show that the variation of the NMP zero estimate is dependent on the nominal voltage and disturbance magnitude. One interpretation of real NMP zero is that for a continuous-time system it is inversely related to the ratio of undershoot and steady-state response for a step response. The previous study showed that the relation is consistent for the discrete-time model of the current flow-actuator system. In other words, segment 2 with a larger NMP zero has a reduced initial reverse response or a larger steady-state lift (or both) in response to a step actuation compared to the other segments. However, the physical implication behind this trend is not clear yet. In addition, as mentioned above, the observation from the previous study based on steady nominal conditions, i.e., the higher the *y*-directional free-stream velocity the larger NMP zero estimate, is different from the current unsteady result.

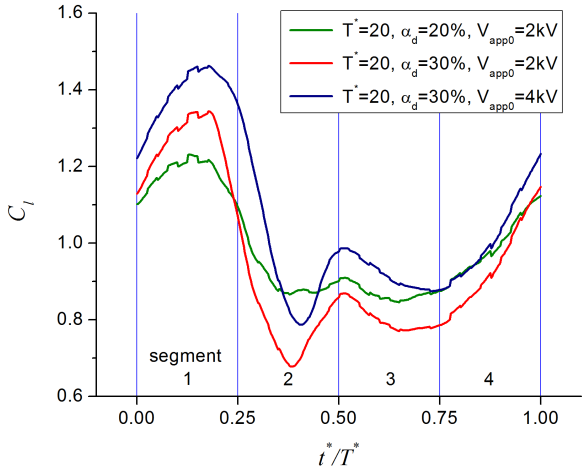

(a) lift variation for one disturbance cycle with the free-stream disturbance and white noise actuation

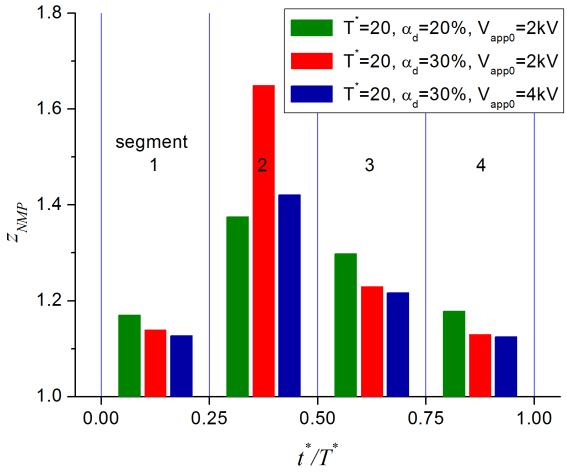

(b) real NMP zero estimates in 4 segments coveing one disturbance cycle

Figure 13 Nonminimum-phase zero estimates for 4 segments in one disturbance period.

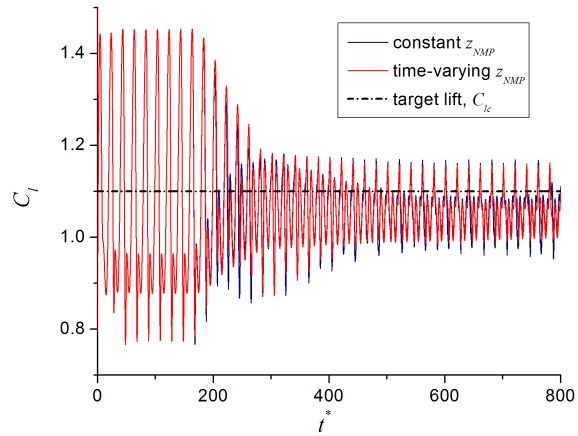

(a) lift time history

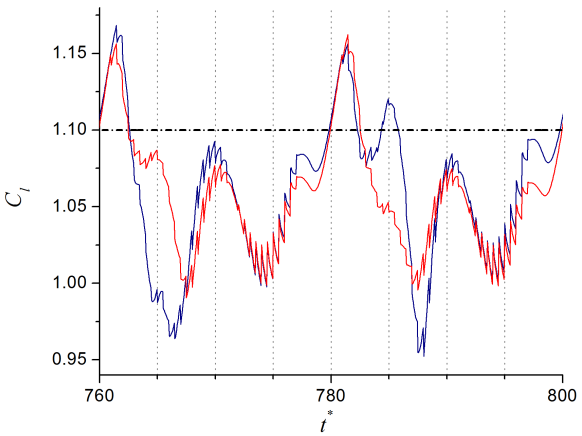

(b) enlarged steady-state from (a)

Figure 14 Closed-loop lift control with and without the time-varying NMP zero: $\alpha_d = 30\%$, $T^* = 20$ ($St = 0.08$, $k = 0.16$), $V_{app0} = 4$ kV, $C_{lt} = 1.1$.

The impact of the application of time-varying NMP zero is shown in Figure 14, compared to the constant NMP zero case. For the same disturbance condition as Figure 12, in order to alleviate the actuator saturation, a higher nominal voltage of 4 kV is used. The controller is turned on at $t^* = 150$. As shown in Figure 14(a), although both the constant and time-varying NMP zero cases show the reduction of the initial lift fluctuation, the latter results in the steady-state response that has a smaller magnitude with higher steadiness. The enlarged time history in Figure 14(b) shows the persisting steady-state lift fluctuation for two disturbance periods. Compared to the constant NMP zero case, it is clear that by introducing the time-varying NMP zero the lift fluctuation is reduced by about 25% mainly in every second quarter period, which corresponds to segment 2 in Figure 13. This partial improvement can be explained by considering the largest variation of the NMP zero in segment 2 that is incorporated in the time-varying NMP zero case.

V. Summary and Conclusions

This study aims at the development of effective flow control framework that can minimize the influence of free-stream unsteadiness at low-Reynolds number applications. More specifically, the control objective is the stabilization of unsteady aerodynamic lift under the influence of unknown wind gusts for the SD7003 airfoil at the chord Reynolds number of 1000. The retrospective cost adaptive control (RCAC) algorithm and general system identification approaches based on linear input-output models are applied to the flow-actuator system that is composed of the airfoil and the dielectric barrier discharge (DBD) actuator on its upper surface. This approach attempts to minimize the requirement for system information, becoming less dependent on unmodeled dynamics, such as the effect of wind gusts. In this study, as a continuation of previous efforts, we focus on the issues with system identification, closed-loop control, and nonlinear flow dynamics for the disturbance with a substantial magnitude that can result in the $O(1)$ variation in the lift coefficient. Major outcomes can be summarized as the followings.

(1) The high-magnitude disturbance induces various sources of nonlinearity in the flow-actuator system. They include the actuator saturation due to the breakdown voltage of the DBD actuator, vortex evolution/shedding mechanisms, and the interaction between the separated flow structure and the unsteady free-stream. Typical characteristics of nonlinear systems, such as the shift of the time-averaged lift (nonlinear steady-state characteristic) and target dependency of the controller's performance, can be identified. In order to handle them, we have explored several treatments including (i) the use of the status of actuator saturation for the controller, (ii) the scaling of the measurement and control to reduce the performance dependency on the learning rate, and (iii) the identification of time-varying system parameters.

(2) Although the flow-actuator system is parameterized based on a time-invariant linear model using impulse response tests, the recursive least squares (RLS) method is applied to include the effect of the unsteady free-stream in the system ID process. The nonminimum-phase (NMP) zero as a representative system parameter is sensitive to the free-stream unsteadiness as well as the identification method. However, for the constant system parameter approach, the controller with the impulse-test-based NMP zero performs better then the one with the RLS method. On the other hand, the RLS method can provide a time-varying NMP zero as mentioned in (4).

(3) The $O(1)$ variation of the lift coefficient is driven by the combination of free-stream fluctuation and the evolution of separated flow region. The closed-loop actuation voltage can successfully reduce the lift fluctuation for the cases with different disturbance periods that span several scenarios of the interaction between free-stream and vortex evolutions. The major control mechanisms are the substantial suppression of vortex evolution processes and the change of the surface pressure through the responsive actuation.

(4) As an effort to reflect the parametric changes due to disturbance in the linear model description, the RLS method is applied to trace the variation of the NMP zero estimate within each disturbance cycle. Since the number of samples within one cycle is not sufficient, out of four segments that compose one disturbance cycle, a concatenated data set for each segment is used to estimate the corresponding NMP zero. The controller with the time-varying NMP zero shows a noticeable improvement in some control results.

Although the current approach proves an effective framework for the control of unsteady aerodynamics, still there are challenges to be addressed as future works. The performance sensitivity to target lift requires a better understanding of the lift stabilization mechanism. In addition, although the controller gains change according to the real system dynamics, which is the key benefit of the adaptive algorithm, the degree of nonlinear effects that can be handled by this adaptive process while relying on the linear model description requires further study. Some cases that show better control results when a time-varying system parameter is used suggest that further improvement is possible through an additional nonlinear process in the control system. Aside from the current flow-actuator system,

since the RLS method can be used for the systems with non-steady nominal state, other flow system subject to dynamic flow separation, such as flapping wings, can be chosen as a flow system in the same framework.

References

[1]Shyy, W., Lian, Y., Tang, J., Viieru, D., and Liu, H., *Aerodynamics of Low Reynolds Number Flyers*, New York, Cambridge Univ. Press, 2008.

[2]Cattafesta, L. N., and Sheplak, M., "Actuators for active flow control," *Annu. Rev. Fluid Mech.*, Vol. 43, 2011, pp. 247-272.

[3]Moreau, E., "Airflow control by non-thermal plasma actuators," *J. Phys. D: Appl. Phys.*, Vol. 40, 2007, pp. 605-636.

[4]Corke, T. C., Enloe, C. L., and Wilkinson, S. P., "Dielectric barrier discharge plasma actuators for flow control," *Ann. Rev. Fluid Mech.*, Vol. 42, 2010, pp. 505-529.

[5]Greenblatt, D., Goksel, B., Rechenberg, I., Schule, C. Y., Romann, D., and Paschereit, C. O., "Dielectric barrier discharge flow control at very low flight Reynolds numbers," *AIAA Journal*, Vol. 46, No. 6, 2008, pp. 1528-1540.

[6]Benard, N., Braud, P., Jolibois, J., and Moreau, E., "Airflow reattachment along a NACA 0015 airfoil by surface dielectric barrier discharge actuator - time resolved particle image velocimetry investigation," *4th Flow Control Conference*, Seattle, Washington, 23-26 June, 2008, AIAA 2008-4202.

[7]Jayaraman, B., Lian, Y., and Shyy, W., "Low-Reynolds number flow control using dielectric barrier discharge actuators," *37th AIAA Fluid Dynamics Conference and Exhibit*, Miami, FL, 25-28 June, 2007, AIAA 2007-3974.

[8]Durscher, R., and Roy, S., "On multi-barrier plasma actuators," *49th AIAA Aerospace Sciences Meeting including the New Horizons Forum and Aerospace Exposition*, Orlando, FL, 4-7 January, 2011.

[9]Hale, C., Erfani, R., and Kontis, K., "Multiple encapsulated electrode plasma actuators to influence the induced velocity: further configurations," *40th Fluid Dynamics Conference and Exhibit*, Chicago, Illinois, 28 June - 1 July, 2010, AIAA 2010-5106.

[10]Zaidi, S. H., Edwards, M. R., Opaits, D. F., and Miles, R. B., "DBD surface charge measurement and mitigation in moving air," *49th AIAA Aerospace Sciences Meeting including the Horizons Forum and Aerospace Exposition*, Orlando, FL, 4-7 January, 2011.

[11]Boesch, G., Vo, H. D., Savard, B., Wanko-Tchatchouang, C., and Mureithi, N. W., "Flight control using wing-tip plasma actuation," *Journal of Aircraft*, Vol. 47, No. 6, 2010, pp. 1836-1846.

[12]Benard, N., and Moreau, E., "Capabilities of the dielectric barrier discharge plasma actuator for multi-frequency excitations," *J. Phys. D: Appl. Phys.*, Vol. 43, 2010, 145201.

[13]Asghar, A., and Jumper, E. J., "Phase synchronization of vortex shedding from two circular cylinders using plasma actuators," *AIAA Journal*, Vol. 47, No. 7, 2009, pp. 1608-1616.

[14]Gillies, E. A., "Low-dimensional control of the circular cylinder wake," *J. Fluid Mech.*, Vol. 371, 1998, pp. 157-178.

[15]Fagley, C. P., Balas, M. J., Siegel, S., Seidel, J., and McLaughlin, T., "Reduced order model of cylinder wake with direct adaptive feedback control," *AIAA Guidance, Navigation, and Control Conference*, Chicago, Illinois, 10-13 August, 2009, AIAA 2009-5856.

[16]Huang, S.-C., and Kim, J., "Control and system identification of a separated flow," *Phys. Fluids*, Vol. 20, 2008, 101509.

[17]Gratton, D., and Willcox, K., "Reduced-order trajectory piecewise-lineare models for nonlinear computational fluid dynamics," *34th AIAA Fluid Dynamics Conference and Exhibit*, Portland, OR, 28 June-1 July, 2004.

[18]Santillo, M. A., Hoagg, J. B., Bernstein, D. S., and Powell, K., "CFD-based adaptive flow control for steady flow field modification," *Proceedings of the 45th IEEE Conference on Decision & Control*, San Diego, CA, 13-15 December, 2006.

[19]Cho, Y.-C., Hoagg, J. B., Bernstein, D. S., and Shyy, W., "Retrospective cost adaptive flow control using a dielectric barrier discharge actuator with parameter-dependent modeling," *49th AIAA Aerospace Sciences Meeting including the New Horizons Forum and Aerospace Exposition*, Orlando, FL, 4-7 Jan, 2011, AIAA 2011-1302

[20]Cho, Y.-C., and Shyy, W., "Adaptive flow control of low-Reynolds number aerodynamics using dielectric barrier discharge actuator," *Prog. Aerosp. Sci*, 2011, doi:10.1016/j.paerosci.2011.06.005.

[21]Santillo, M. A., and Bernstein, D. S., "Adaptive control based on retrospective cost optimization," *Journal of Guidance, Control, and Dynamics*, Vol. 33, No. 2, 2010, pp. 289-304.

[22]Ljung, L., and Soderstrom, T., *Theory and Practice of Recursive Identification*, Cambridge, The MIT Press, 1983.

[23]Cho, Y.-C., Fledderjohn, M., Holzel, M., Jayaraman, B., Santillo, M., Bernstein, D. S., and Shyy, W., "Aadptive flow control of low Reynolds number aerodynamics using a dielectric barrier discharge actuator," *47th AIAA Aerospace Sciences Meeting Including The New Horizons Forum and Aerospace Exposition*, Orlando, FL, 5-8 January, 2009, AIAA 2009-378.

[24]Cho, Y.-C., Hoagg, J. B., Bernstein, D. S., and Shyy, W., "Retrospective cost adaptive control of low-Reynolds number aerodynamics using a dielectric barrier discharge actuator," *40th Fluid Dynamics Conference and Exhibit*, Chicago, IL, 28 June-1 July, 2010, AIAA 2010-4841.

[25]Kamakoti, R., Thakur, S., Wright, J., and Shyy, W., "Validation of a new parallel all-speed CFD code in a rule-based framework for multidisciplinary applications," *36th AIAA Fluid Dynamics Conference and Exhibit*, San Francisco, CA, 5-8 June, 2006, AIAA 2006-3063.

[26]Shyy, W., Jayaraman, B., and Andersson, A., "Modeling of glow discharge-induced fluid dynamics," *J. Appl. Phys.*, Vol. 92, No. 11, 2002, pp. 6434-6443.

[27]Jayaraman, B., Cho, Y.-C., and Shyy, W., "Modeling of dielectric barrier discharge plasma actuator," *J. Appl. Phys.*, Vol. 103, 2008, 053304.

[28]Grundmann, S., Klumpp, S., and Tropea, C. "Experimental and numerical investigations of boundary-layer influence using plasma-actuators," *Active Flow Control, NNFM 95*. Springer, New York, 2007, pp. 56-68.
[29]Skogestad, S., and Postlethwaite, I., *Multivariable Feedback Control: Analysis and Design*, New York, John Wiley & Sons, 1996.
[30]Leon de la Barra S., B. A., "On undershoot in SISO systems," *IEEE Trans. Autom. Control*, Vol. 39, No. 3, 1994, pp. 578-581.
[31]Coffer, B. J., Hoagg, J. B., and Bernstein, D. S., "Cumulative retrospective cost adaptive control of systems with amplitude and rate saturation," *2011 American Control Conference*, San Francisco, CA, 29 June-1 July, 2011.
[32]Haber, R., "Nonlinearity tests for dynamic processes," *7th IFAC/IFORS Symposium on Identification and System Parameter Estimation*, York, UK, 1985, pp. 409-414.